Available online at www.sciencedirect.com

jmr&t Journal of Materials Research and Technology

journal homepage: www.elsevier.com/locate/jmrt

Original Article

Influence of processing temperature on microhardness evolution, microstructure and superplastic behaviour in an Al–Mg alloy processed by high-pressure torsion

Denise C. Machado [a], *Paula Cibely Alves Flausino* [b], *Yi Huang* [c,d], *Paulo Roberto Cetlin* [e], *Terence G. Langdon* [c], *Pedro Henrique R. Pereira* [f,*]

[a] *Graduate Program in Metallurgical, Materials and Mining Engineering, Universidade Federal de Minas Gerais, Belo Horizonte, 31270-901, MG, Brazil*

[b] *Department of Metallurgical and Materials Engineering, Universidade Federal de Ouro Preto, Ouro Preto, 35400-000, MG, Brazil*

[c] *Materials Research Group, Department of Mechanical Engineering, University of Southampton, Southampton, SO17 1BJ, UK*

[d] *Department of Design and Engineering, Faculty of Science and Technology, Bournemouth University, Poole, Dorset, BH12 5BB, UK*

[e] *Department of Mechanical Engineering, Universidade Federal de Minas Gerais, Belo Horizonte, 31270-901, MG, Brazil*

[f] *Department of Metallurgical and Materials Engineering, Universidade Federal de Minas Gerais, Belo Horizonte, 31270-901, MG, Brazil*

ARTICLE INFO

Article history:
Received 24 January 2023
Accepted 22 March 2023
Available online 27 March 2023

Keywords:
Aluminium alloys
Hardness
High-pressure torsion
Superplasticity
Thermal stability

ABSTRACT

Experiments were conducted to assess the effect of processing temperature on the hardness evolution, microstructure and the flow properties of an annealed Al–3Mg alloy processed by high-pressure torsion (HPT) at either 300 or 450 K. The results demonstrate that HPT processing at room temperature (*RT*) leads to higher microhardness values with a more uniform hardness distribution in the Al alloy compared with processing at 450 K. After 10 HPT turns at *RT*, the microstructure displayed a more intense grain refinement, a higher dislocation density and smaller Al_3Mg_2 precipitates than after HPT at 450 K. Accordingly, the metal processed at *RT* showed enhanced strength at *RT* and consistently exhibited superplastic flow during deformation at 523 K, with tensile elongations of ~530–650% for strain rates from 10^{-3} to 10^{-2} s^{-1}. Conversely, a maximum elongation of ~110% was recorded at 523 K in the alloy processed by HPT at 450 K. This behaviour is attributed to an enhanced thermal stability in the metal processed at *RT* compared with HPT at 450 K where deformation at 523 K led to the onset of abnormal grain coarsening due to a more

* Corresponding author.
E-mail address: ppereira@demet.ufmg.br (P.H.R. Pereira).

https://doi.org/10.1016/j.jmrt.2023.03.167

disperse distribution of grain sizes and the partial dissolution and coalescence of Al_3Mg_2 precipitates after HPT processing.

1. Introduction

Severe Plastic Deformation (SPD) procedures have been widely used to produce metals with ultrafine grains (<1 μm) [1,2] and thus excellent load-bearing capacities at low homologous temperatures due to Hall-Petch strengthening [3,4]. Despite the wide variety of SPD methods, high-pressure torsion (HPT) [5,6] is an important procedure because it requires a relatively simple experimental apparatus [7,8] and it permits the imposition of high hydrostatic compressive pressures concurrently with torsional straining under the control of the processing temperature [9–12]. In processing through HPT using quasi-constrained anvils [13,14], disc-shaped samples are compressed between two anvils and severely strained by the imposition of torsional stresses through the rotation of either the upper or lower anvil.

The high internal energy stored in HPT-processed metals because of their high densities of grain boundaries and dislocation structures increases the susceptibility of the microstructures to undergo early recrystallization at relatively low temperatures [15,16]. Therefore, different strategies have been carried out to improve the microstructural stability of materials processed by SPD such as (i) the development of alloys containing elements which originate as nanosized precipitates during heating [17–20], (ii) the application of SPD procedures at warm conditions [21–25], (iii) the use of cyclic deformation with low strain amplitudes [26–28] and (iv) the formation of nanosized particles and solute segregation at grain boundaries concurrently with deformation in microstructures having secondary phases prior to processing [29–35].

The additions of Sc in Al alloys enhance the stabilities of the Al matrices during heating due to the formation of Al_3Sc dispersoids [36,37]. Accordingly, SPD-processed Al–Mg–Sc alloys can retain ultrafine grains at temperatures suitable for achieving optimum superplastic flow [18,22,38–45]. After processing by 8 passes of equal-channel angular pressing (ECAP) at room temperature (*RT*) an Al–3Mg–0.2Sc alloy achieved a maximum elongation of ~2580% at 723 K for an initial strain rate of 3.3×10^{-3} s^{-1} [42]. Furthermore, a record elongation of ~4100% was attained in the Al–5Mg–0.2Sc–0.08Zr alloy processed through 10 ECAP passes at ~600 K, although this led to larger grain sizes than for alloys with similar compositions processed by ECAP at *RT* [44,46,47].

The influence of processing temperature on the flow properties and thermal stability of Al–Mg–Sc alloys as also been examined after HPT processing [21,22,48,49]. It was demonstrated that the application of this procedure at either 300 or 450 K promotes further grain refinement compared with ECAP and permits the achievement of low temperature superplasticity with elongations higher than after ECAP for comparable miniature tensile specimens [22,41,45].

HPT processing may lead to fragmentation and partial dissolution of large secondary phases in Al alloys [35,50,51]. This may also be followed by solute segregation at grain boundaries and/or precipitation of nanoparticles concurrently with deformation [29,34,52–54]. These microstructural characteristics reveal a potential for improving the microstructural stability of Al alloys due to grain boundary stabilisation [32,55–57] and thereby permit the achievement of superplastic ductilities in commercially available alloys without the addition of any costly elements.

Accordingly, the present research was designed specifically to investigate the effect of the processing temperature on microstructural evolution, hardening and superplastic properties of an Al–3Mg alloy processed by HPT at either 300 or 450 K. To enhance the microstructural stability through the development of fragmented second-phase particles, the Al alloy was annealed before the HPT processing.

2. Experimental material and procedures

An Al–3%Mg alloy (% in weight) was used in the current investigation. This alloy was received in the form of bars having 10 mm in diameter. The bars were annealed at 773 ± 2 K for 1 h and air cooled to develop a homogeneous array of grains with an average size of ~300 μm as determined by the linear intercept method.

The annealed billets were cut into discs with thicknesses of ~1 mm and ground using abrasive papers to a thickness of ~0.85 mm. Afterwards, they were processed through 0.5, 1, 2, 5, 10 and 20 HPT revolutions (*N*) at either room temperature (~300 K) or 450 ± 5 K using quasi-constrained anvils [8,13,14] under a nominal pressure of 6.0 GPa and a rotation rate of ~2 rpm. The temperature of ~450 K was achieved by incorporating small heating elements around the anvils and the temperature was controlled by a thermocouple placed within the upper anvil at a position ~10 mm from the HPT sample as described in earlier studies [58,59]. To decrease the temperature gradient between the workpiece and the anvils during processing at ~450 K, each disc was compressed within the anvils and held at the HPT facility for ~10 min prior to application of the compression-torsion stage [9].

The surfaces of the annealed sample and the HPT-processed Al–3Mg discs were ground and polished using 9, 3 and 1 μm diamond paste. Then the entire surfaces of these HPT and annealed specimens were examined through X-Ray Diffraction (XRD) employing a Philips PANalytical diffractometer with Cu Kα radiation (λ = 1.5406 Å), using a scanning angle range 2θ from 10 to 90° and a step size of 0.02°. The instrumental profile was determined using Lanthanum Hexaboride (LaB_6) powder and the diffractograms were applied to estimate the area-weighted crystallite size $\langle x_{área} \rangle$ and the dislocation density (ρ) using the Convolutional Multiple Whole Profile (CMWP) software as described elsewhere [60].

Microhardness measurements were taken at the middle-sections of the polished discs using an FM-700 tester equipped with a Vickers indenter operating under a load of 100 gf and a dwell time of 10 s. The hardness distribution was determined along the disc diameter using the same procedure described in previous studies [48,61] where the average microhardness at each position and its standard deviation were calculated using the values recorded at 4 equidistant indentations.

Microstructural analyses through Transmission Electron Microscopy (TEM) were performed on the Al–3Mg discs processed by 10 revolutions using an FEI Tecnai G2-12-Spirit Biotwin microscope, operating under 120 kV. TEM lamellae were extracted from the discs at positions located at ~3 mm from their centres applying focused ion beam milling using an FEI Quanta 3D FEG microscope.

The deformation behaviours of the Al–3Mg alloy processed by 10 HPT turns were assessed by tensile testing using a Shimadzu Autograph AGS-X universal tester. After processing, the surfaces of the discs became curved due to the elastic distortion of the HPT anvils [9]; accordingly, to obtain flat surfaces, the samples were ground and polished to a thickness of ~0.60 mm. Thereafter, using the same procedure described earlier [41,62–64], two miniature off-centre tensile specimens with widths and gauge lengths of ~1.0 and 1.1 mm, respectively, were cut from each disc using electron discharge machining and subsequently they were polished to obtain mirror-like surfaces along the gauge areas. These samples were tested at *RT* using a constant crosshead speed to give an initial strain rate ($\dot{\varepsilon}$) of 1.0×10^{-3} s^{-1} and also at 523 ± 2 K at strain rates of $\sim 1.0 \times 10^{-3}$, 3.3×10^{-3} and 1.0×10^{-2} s^{-1}. Following tensile testing at 523 K, the topography in the gauge section of the specimens was analysed through Scanning Electron Microscopy (SEM) using an FEI Quanta 200 FEG microscope and the resultant images were used to estimate the grain sizes applying the linear intercept method.

3. Experimental results

3.1. Microhardness variations

Fig. 1 shows the variation of the microhardness along the mid-section of discs of the Al–3Mg alloy in the undeformed condition and after processing for up to 20 HPT revolutions at either 300 or 450 K. It follows from Fig. 1(a) that the annealed alloy displays a reasonably homogeneous distribution of hardness with an average value of ~55 HV. After 1/2 turn at *RT*, there is a marked increase in the microhardness values involving a minimum hardness of ~80 HV at the disc centre which rises to ~160 HV at the edges. Additional straining leads to a gradual increase in the hardness values in the central area such that, similar to an earlier study [65], the material subjected to 10 revolutions exhibits a Vickers microhardness of ~180 HV over the entire disc diameter. The microhardness continues to rise slightly and achieves an average value of ~200 HV after 20 turns.

A comparison of Fig. 1(a) and (b) shows that the Al–3Mg alloy processed at 450 K achieves much lower hardness values than the same material processed by HPT at *RT*. After 1/2 turn at 450 K, the Vickers microhardness ranges from ~80 to 120 HV for positions located at the centre and near to the disc periphery, respectively. The distributions of microhardness values remain essentially unchanged after processing through 1, 2 and 5 HPT revolutions at 450 K. It is also noted that the microhardness saturates at ~125 HV at the sample edges and, even though there is a slight increase in hardness in the central region of the discs after 10 and 20 turns, the distribution remains inhomogeneous where this contrasts with the results obtained for HPT at *RT*.

3.2. Microstructural evolution

The XRD profiles of the Al–3Mg disc before and after various numbers of HPT turns are shown in Fig. 2 where the profile

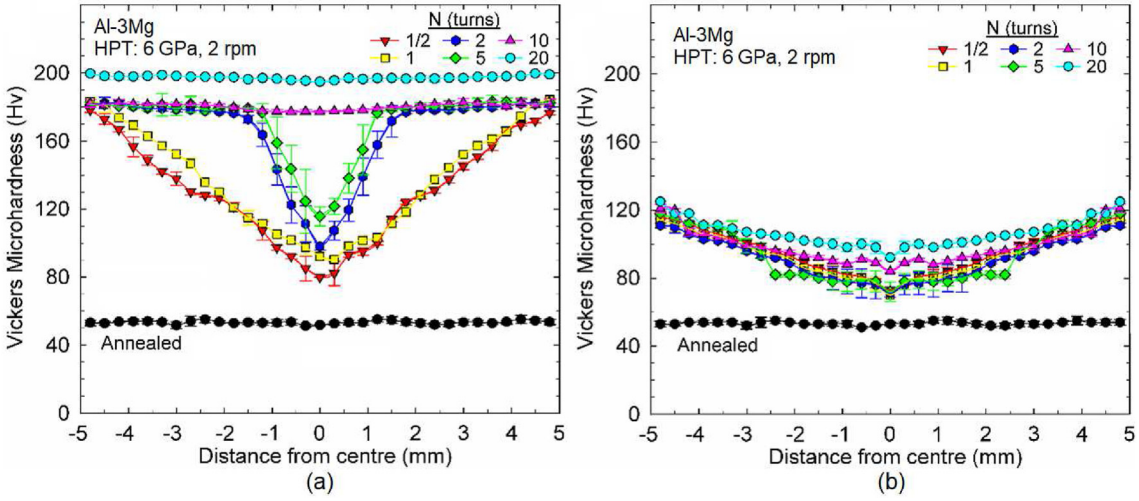

Fig. 1 – Variation of Vickers microhardness recorded at the mid-section positions with distance from the centre of Al–3Mg discs processed by HPT at either (a) 300 or (b) 450 K.

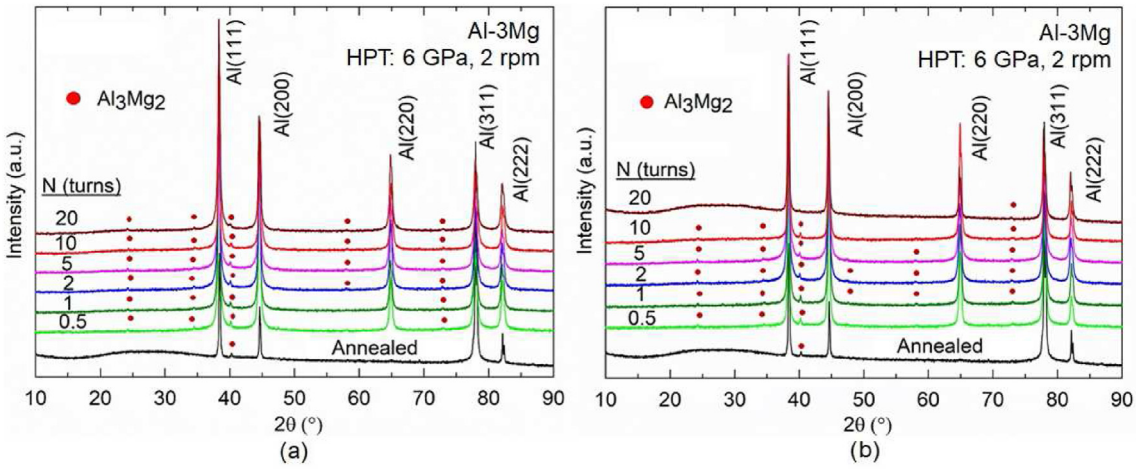

Fig. 2 – XRD patterns for the Al–3Mg alloy processed by HPT at either (a) 300 or (b) 450 K.

labelled "Annealed" corresponds to the unprocessed material. The curves in Fig. 2 indicate that the peak positions are not significantly affected by HPT processing but nevertheless the XRD peaks display a marked broadening after HPT especially when processing at *RT*. The annealed material exhibits peaks for the (200), (111) and (222) planes of the Al matrix and there is also a peak at $2\theta \approx 40.3°$ which suggests the presence of a second phase.

HPT processing at either 300 or 450 K leads to the onset of a peak corresponding to the (220) plane in the Al matrix. Furthermore, as the number of turns increases so the XRD patterns exhibit additional peaks following a pattern expected for the Al_3Mg_2 phase. However, after $N > 5$ for HPT at 450 K some of the secondary phase peaks disappear or became blurred and undetectable. This may be attributed to either gradual fragmentation and/or a partial dissolution of the Al_3Mg_2 phases [66–68].

The XRD profiles were evaluated using the CMWP software. The results are shown in Fig. 3 which displays the variations of the average crystallite size and the dislocation density in the Al–3Mg alloy with the numbers of HPT turns. The undeformed alloy ($N = 0$) exhibits $x_{<area>} \approx 1000$ nm and $\rho \approx 1 \times 10^{12}$ m^{-2}. It follows from Fig. 3 that the average crystallite size decreases rapidly with increasing numbers of revolutions until there is an apparent saturation at minimum values of ~140 nm and 240 nm for the Al alloy processed by HPT at 300 and 450 K, respectively.

The results in Fig. 3(b) reveal that, by comparison with the as-annealed condition, the dislocation density increases by about two orders of magnitude after 1/2 HPT revolutions at 300 K, reaching ~4×10^{14} m^{-2}. The ρ values then increase at a lower rate to ~9×10^{14} m^{-2} after 5 turns and they remain nearly constant up to 20 HPT revolutions. It should be noted that the values for the dislocation density in this study show the same trend as in a recent study even though a different method was used to estimate ρ [65].

It is surprisingly shown in Fig. 3(b) that the Al–3Mg alloy processed through ½ turn of HPT at 450 K exhibits a higher dislocation density (~10^{15} m^{-2}) after HPT at *RT* at an equivalent condition. Further straining leads to a rapid reduction in the density of dislocations which becomes lower than in the Al–3Mg alloy processed by HPT at *RT*. After 10 HPT turns at 450 K, $\rho \approx 3 \times 10^{14}$ m^{-2} and thereafter it drops only marginally up to 20 revolutions.

Figs. 4 and 5 present typical TEM images taken at positions located at ~ 3.5 mm from the centres of Al–3Mg discs processed by 10 turns of HPT at 300 and 450 K turns, respectively. For simplification, the Al–3Mg discs subjected to 10 turns of HPT at either 300 or 450 K are henceforth denoted 10-HPT-RT and 10-HPT-HT, respectively. Inspection of Fig. 4(a) and (b) reveals that, for both processing temperatures, HPT processing promoted the development of ultrafine-grained structures in the Al–3Mg alloy.

The microstructure of the 10-HPT-RT material has slightly elongated grain structures with an average size of ~150 nm, where this is similar to earlier investigations after processing different Al–3Mg alloys by HPT at *RT* [22,45,48,69,70]. Additionally, the clearly defined rings in the SAED pattern in Fig. 4(a) suggest that the domains in Fig. 4(a) are highly misoriented and therefore are predominantly grains and not subgrains. Conversely, the Al–3Mg alloy processed by HPT at 450 K exhibits fairly equiaxed grains with an average size of ~500 nm. It is important to note that this value is much larger than the grain size reported for an Al–3Mg–0.2Sc alloy subjected to 10 turns of HPT at the same temperature although the latter alloy was solution treated prior to processing [21,22]. Furthermore, based on the ring-like shape of the SAED pattern for the 10-HPT-HT disc and considering the smaller number of crystals in the examined area, it is also likely that the structures in Fig. 4(b) are mostly separated by high-angle grain boundaries.

It is apparent from the higher magnification TEM images in Fig. 5 that the HPT-processed alloy exhibits dislocation structures and a large number of second-phase particles within the newly developed grains. The presence of free and tangled dislocations is more evident in the alloy processed at 450 K, as noted in Fig. 5(c) and (d). These dislocations are often held up by the nanosized particles which correspond to Al_3Mg_2 precipitates as shown by the XRD analyses in Fig. 2. The average equivalent diameter of these round-shape

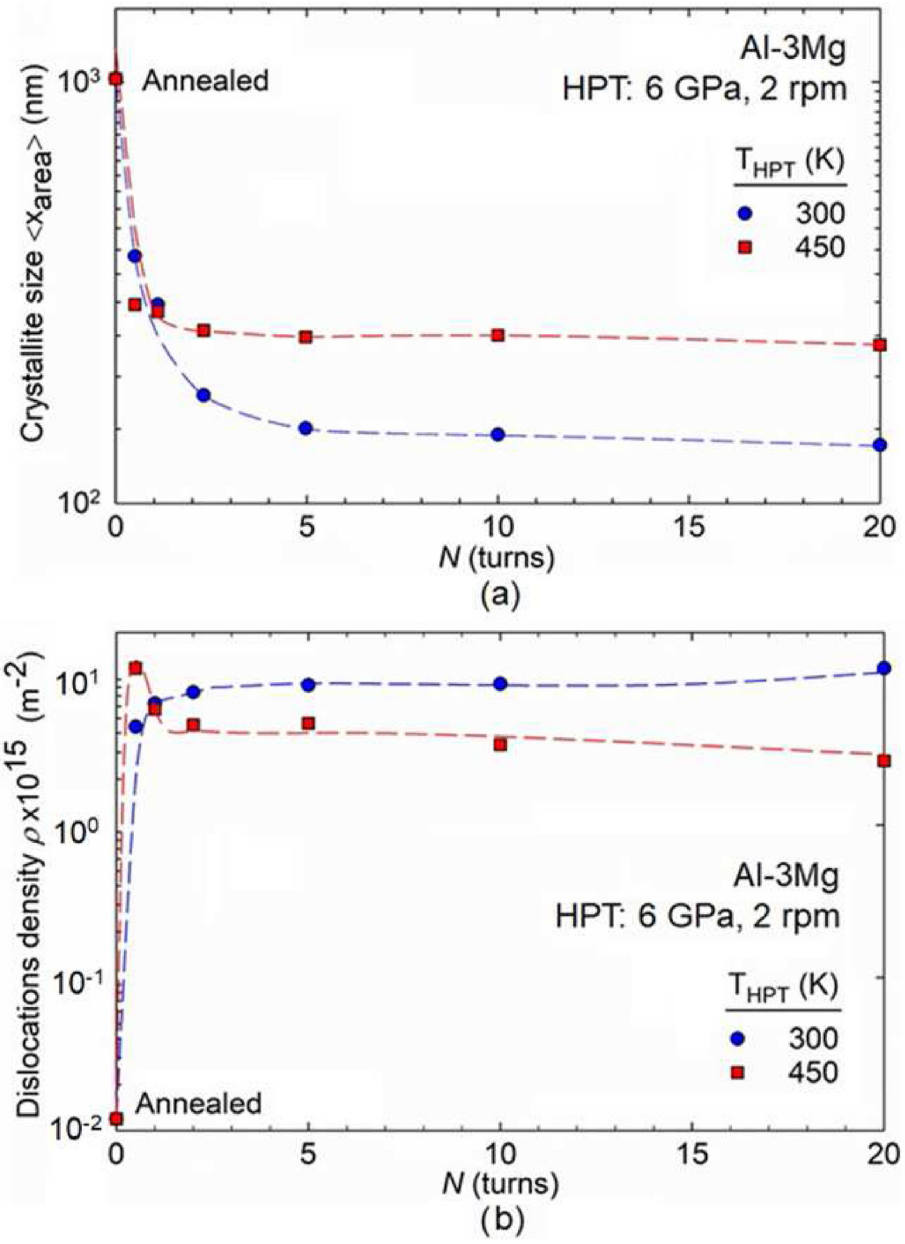

Fig. 3 – (a) Crystallite size and (b) dislocation density as a function of number of turns for Al–3Mg discs processed by HPT at either (a) 300 or (b) 450 K.

particles was estimated using a procedure involving a measurement of the area of >300 precipitates, and this gave values of ~10 and ~16 nm for the Al–3Mg alloy processed through 10 turns of HPT at 300 K and 450 K, respectively.

3.3. *Tensile properties and microstructure after testing*

Samples of the Al–3Mg alloy subjected to 10 HPT turns at either 300 or 450 K were tested in tension at 300 and 523 K using different strain rates. Fig. 6 shows a representative plot of engineering stress vs engineering strain for the HPT-processed alloy pulled to failure at *RT* using a strain rate of 10^{-3} s^{-1}. The results demonstrate that the alloy processed by HPT at 450 K displays lower flow stresses, but a markedly higher elongation when compared with the 10-HPT-RT material. The latter reached a significantly higher engineering stress without noticeable deformation, indicating a brittle behaviour under tensile stresses. Analogous results were reported recently for an Al–4.4Mg–0.26Sc–0.09Zr alloy [71] processed by 10 HPT revolutions at different temperatures and tensile tested at similar conditions. However, the Al–3Mg in the present study exhibits a lower yield stress and enhanced ductility after HPT at 450 K.

Fig. 7(a) shows plots of true stress vs true strain for samples processed by 10 HPT turns at 300 and 450 K and further pulled to failure at 523 K using strain rates varying from 1.0×10^{-3} to 1.0×10^{-2} s^{-1}. These plots were obtained from data acquired using miniature specimens after the elimination of the elastic

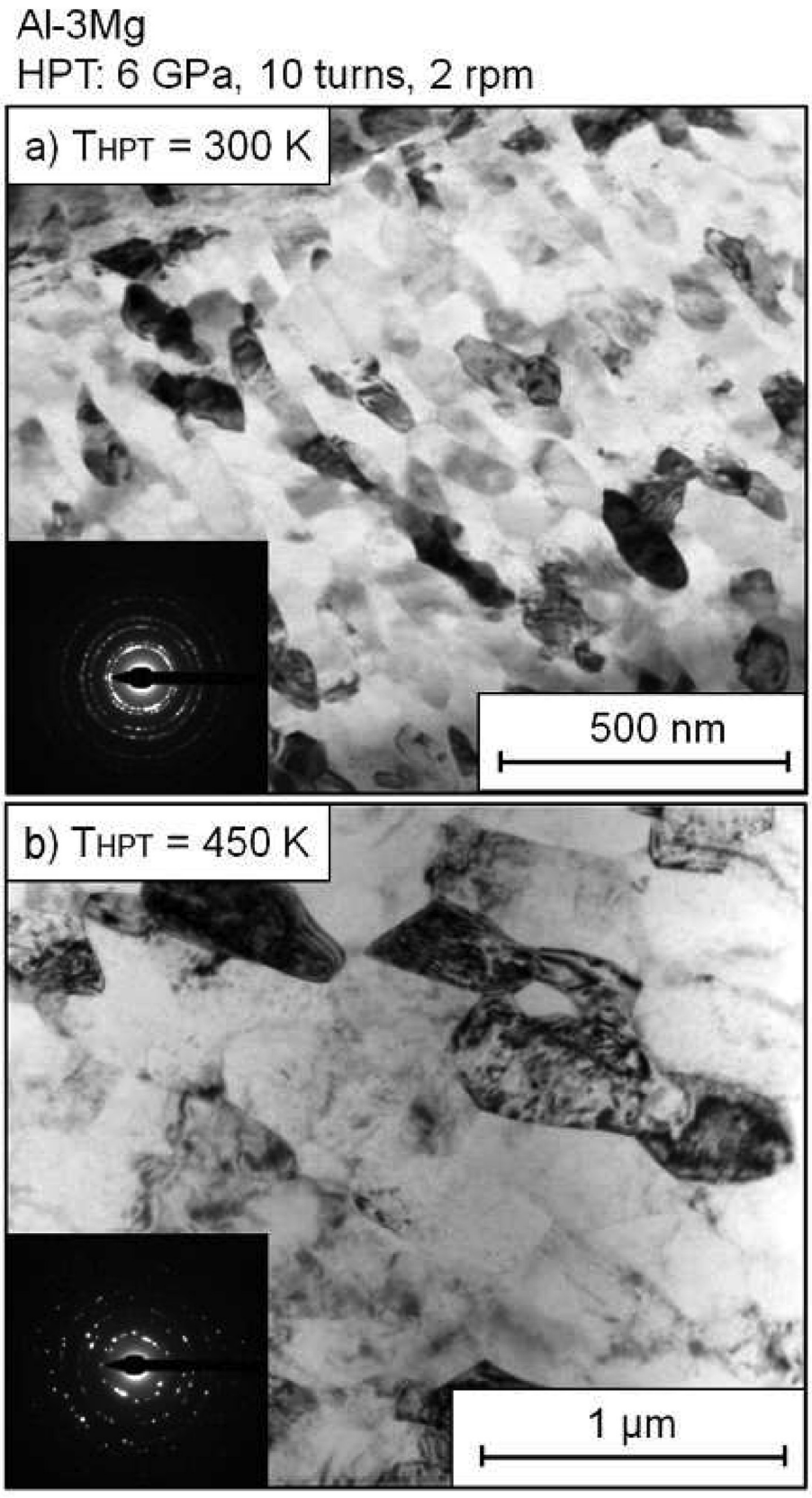

Fig. 4 – TEM images and corresponding SAED patterns showing grains and dislocation structures of the Al–3Mg alloy processed by 10 HPT turns at either (a) 300 or (b) 450 K.

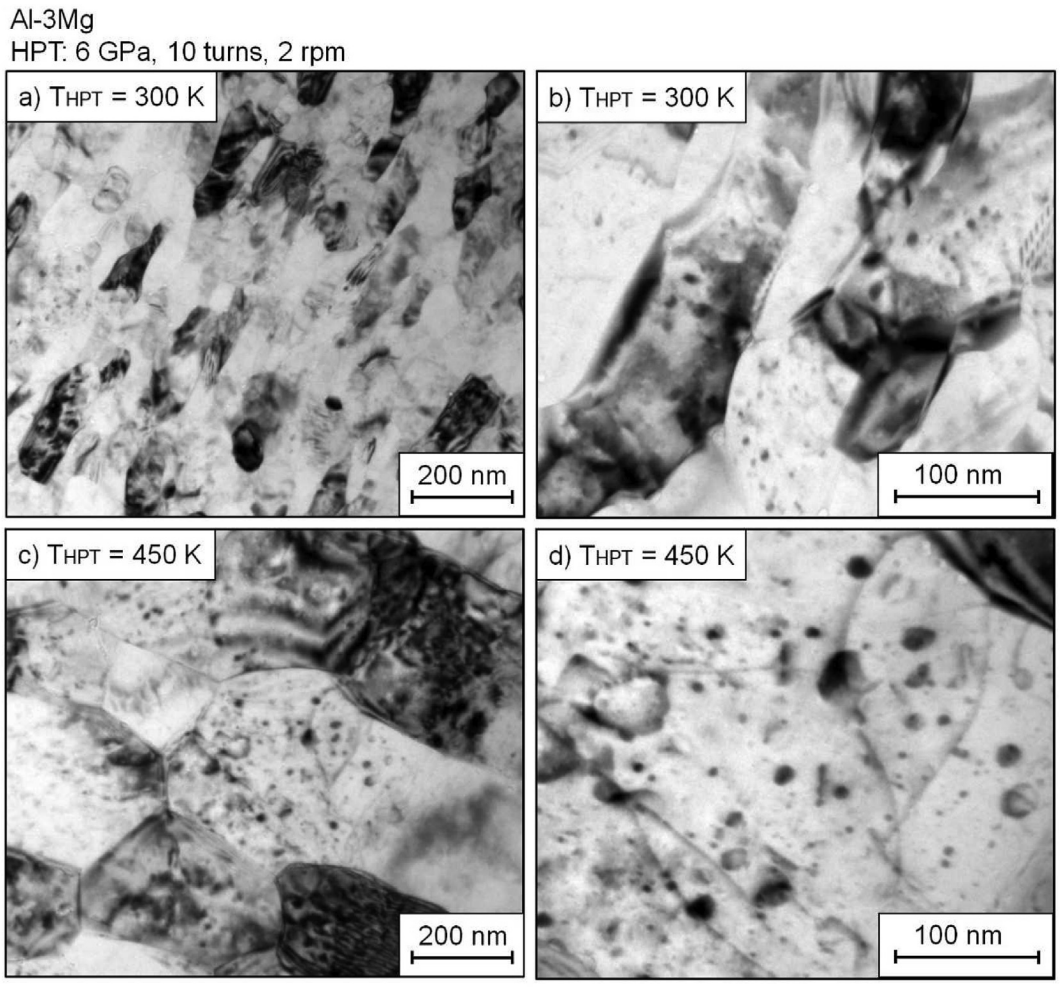

Fig. 5 – TEM images revealing the presence of precipitates for the Al–3Mg alloy processed by 10 turns of HPT at either (a and b) 300 or (c and d) 450 K.

deformation from the testing apparatus and, in addition, the occurrence of uniform straining was assumed to convert engineering stress into true stress. Accordingly, the values of true stress at strains beyond the maximum stress do not reflect the true flow behaviour.

Inspection of Fig. 7(a) shows that increasing the testing temperature from 300 to 523 K using a strain rate of 1.0×10^{-3} s^{-1} leads to higher elongations but significantly lower stress levels for the HPT-processed alloy. It is apparent from the curves in Fig. 7(a) that, for comparable strain rates, the metal processed by HPT at *RT* displays significant work hardening whereas the alloy processed at 450 K exhibits only minor strain-hardening and achieves lower maximum strains. The results in Fig. 7(a) also reveal an unusual increase in ductility for the Al–3Mg processed by HPT at *RT* after increasing the deformation temperature from 300 to 523 K: true strains above ~1.8 are now attained during tensile testing with a maximum strain of ~2.0 for $\dot{\varepsilon} \approx 10^{-3}$ s^{-1}.

Fig. 7(b) shows the variation of the flow stress at $\varepsilon = 0.1$ with the initial strain rate for samples processed by 10 HPT turns at either at 300 or 450 K. The experimental datum points in Fig. 7(b) were plotted using log scales for both the true strain rate and the true stress so that the slopes of these curves correspond to the apparent strain rate sensitivity (m) and provide information on the predominant deformation mechanisms [72]. It is readily noted that the 10-HPT-HT material exhibits higher flow stresses at $\varepsilon = 0.1$ when compared with the 10-HPT-RT alloy under equivalent conditions. In addition, the slope of the curve increases with decreasing HPT temperature such that $m \approx 0.5$ for the 10-HPT-RT metal at 523 K within the range of strain rates used in this study.

Fig. 8 shows the shapes of the Al–3Mg specimens after high temperature tensile testing for the material originally subjected to 10 turns of HPT processing at either 300 or 450 K. The elongation values are also displayed on the right side of the deformed samples. It follows from Fig. 8 that the Al–3Mg alloy processed by 10 turns of HPT at *RT* achieves higher tensile elongations than the 10-HPT-HT samples at 523 K. The images in Fig. 8 reveal that superplastic elongations, defined as elongations to failure greater than 400% [73,74], are consistently attained in the 10-HPT-RT samples over the entire range of strain rates used in this study. Conversely, elongations ranging from ~70% to 110% were reached in the 10-HPT-HT samples tested at 523 K. A more detailed examination of these

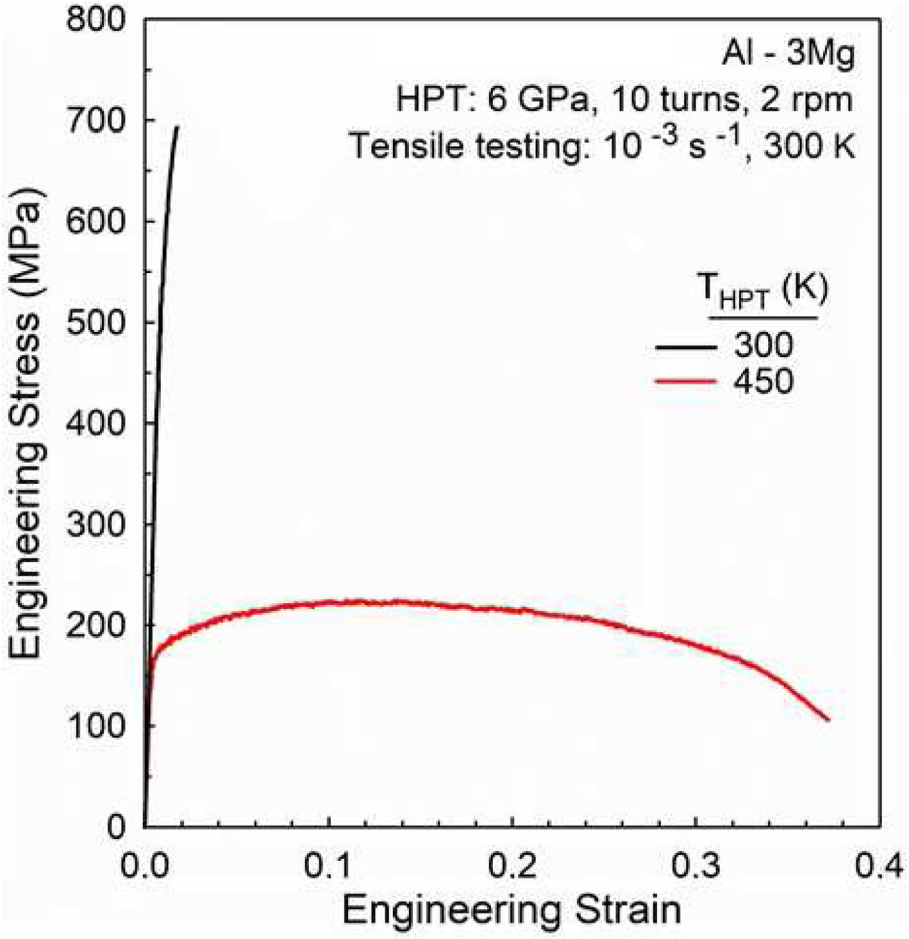

Fig. 6 – Engineering stress vs. engineering strain curves for the Al–3Mg alloy processed by HPT at either 300 or 450 K and further tested in tension at 10^{-3} s^{-1} at 300 K.

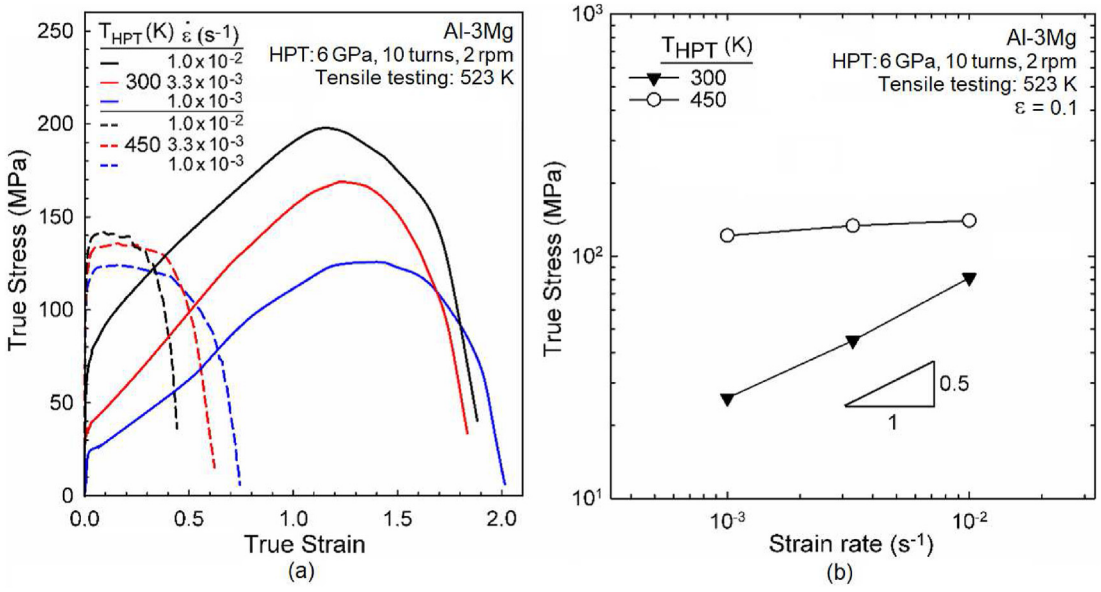

Fig. 7 – (a) True stress vs true strain and (b) true stress at $\varepsilon = 0.1$ vs strain rate curves of the Al–3Mg alloy processed by HPT at either 300 or 450 K and subsequently tensile tested at 523 K using strain rates of 1.0×10^{-2}, 3.3×10^{-3} and 1.0×10^{-3} s^{-1}.

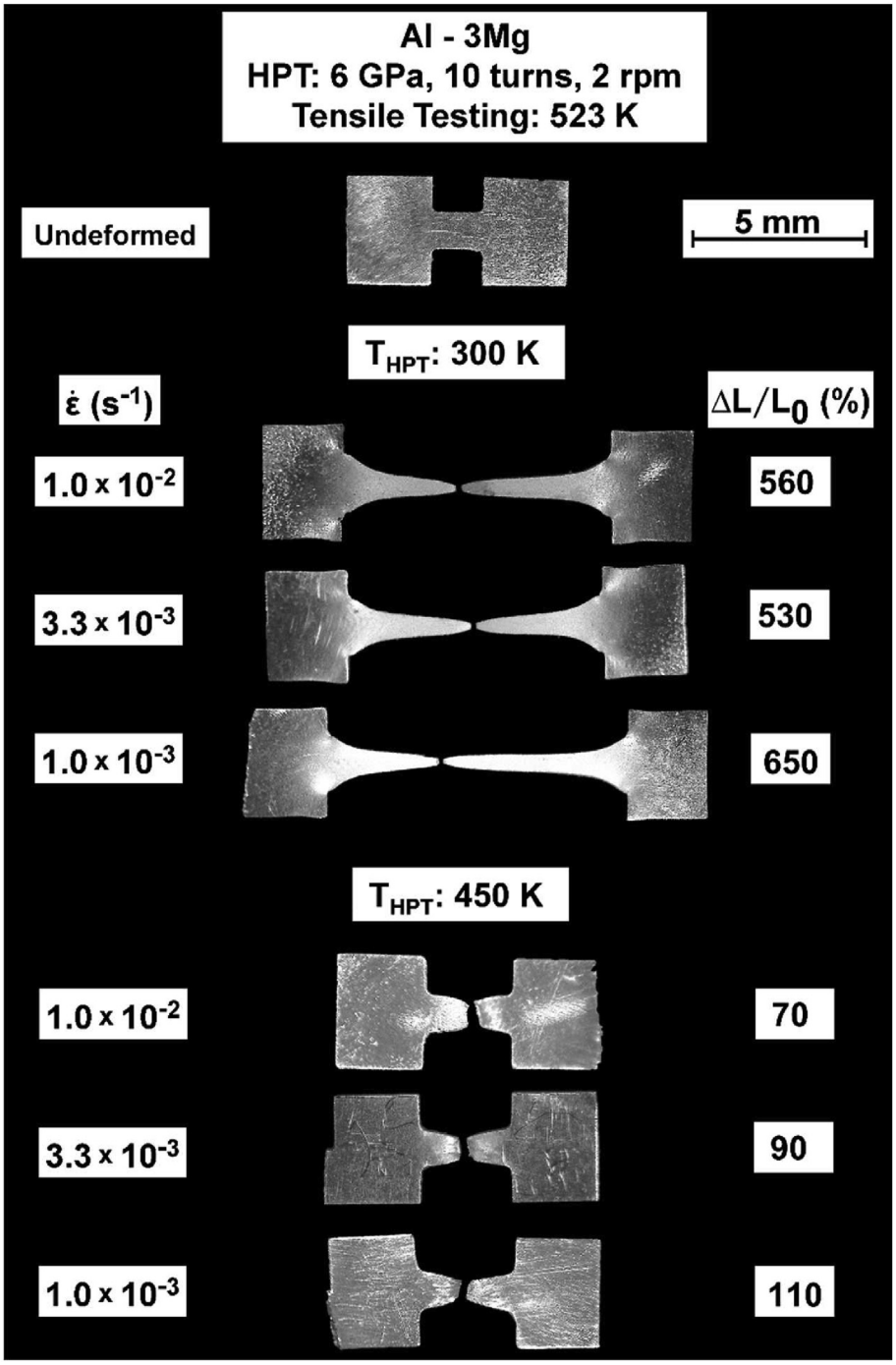

Fig. 8 – Shape of samples of the Al–3Mg alloy processed through 10 turns of HPT at either 300 or 450 K and subsequently pulled to failure at 523 K.

images reveals that for all conditions the width of the miniature specimens exhibits evidence of a localized necking in the vicinity of their fracture tip, but this corresponds to a smaller region compared to the total gauge area in the 10-HPT-HT specimens.

Superplasticity occurs through the movement of neighbouring grain boundaries through grain boundary sliding (GBS) [75] and this means the grain structures stand out on the surfaces of specimens during tensile testing. Accordingly, to assess the size and distribution of the grains at the surfaces of the tested specimens, Fig. 9 shows SEM images of the surface topographies in the gauge areas of Al–3Mg specimens processed by 10 HPT turns and tensile tested at 523 K using strain rates of 10^{-3} and 10^{-2} s^{-1}.

It is clearly visible in the SEM images in Fig. 9(a) and (b) that the 10-HPT-RT alloy exhibits uniform microstructures formed by nearly equiaxed grains with average sizes ($\overline{L}$) of ~1.0 and 2.0 μm, as estimated for the specimens tested at 10^{-2} and 10^{-3} s^{-1}, respectively. By contrast, the microstructures of the material processed by HPT at 450 K and subsequently tested in

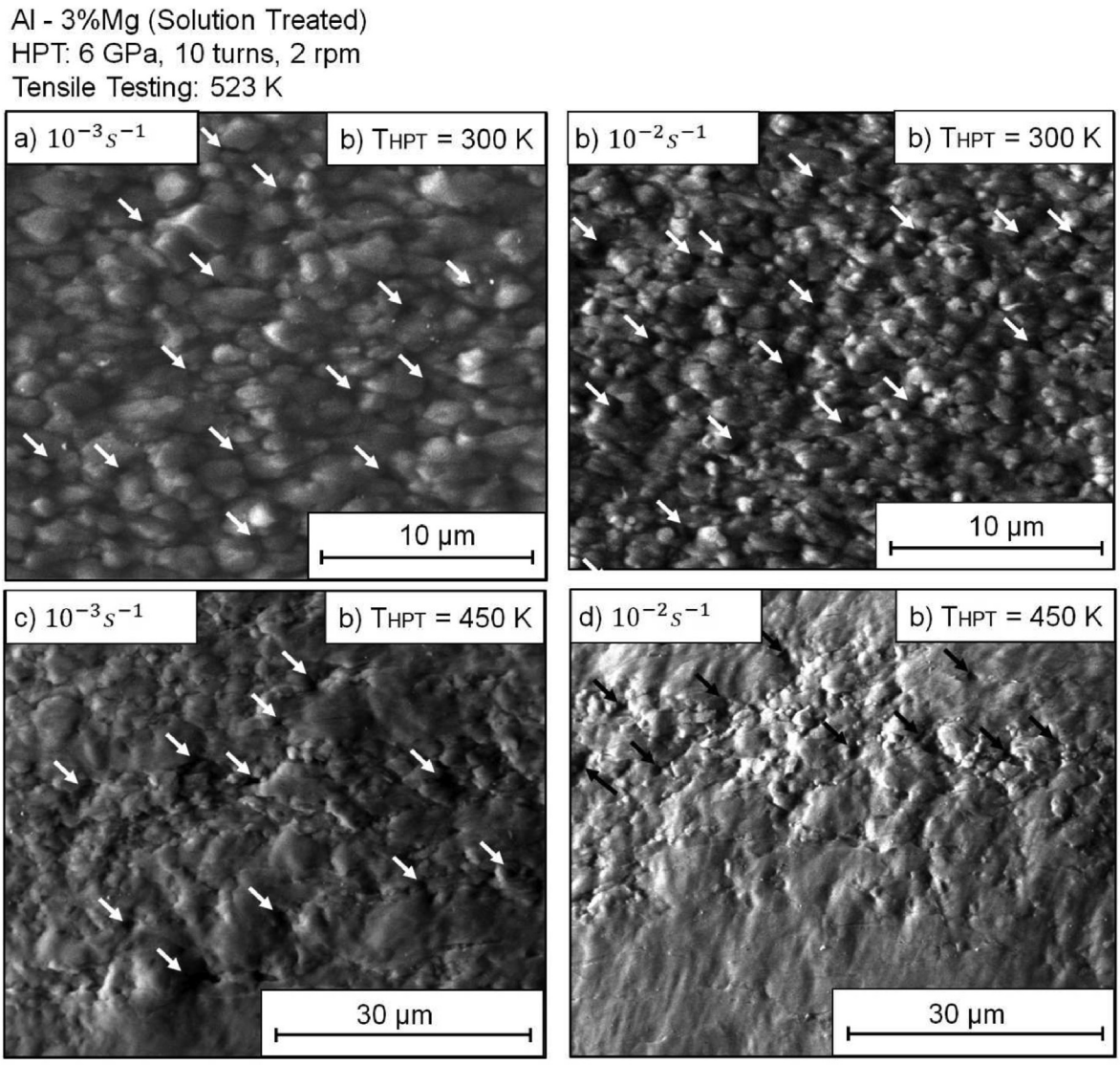

Fig. 9 – SEM images taken along the gauge area of Al–3Mg specimens processed through 10 turns of HPT at either (a and b) 300 or (c and d) 450 K and further tested in tension at 523 K at strain rates of 10^{-3} and 10^{-2} s^{-1}.

tension are very inhomogeneous and their grain structures can be divided into two separate groups. As shown in Fig. 9(c) and (d), some of the grains are nearly equiaxed and have diameters of the order of a few micrometres. However, these grain structures are intermixed with much larger grains giving rise to a bimodal structure with $\overline{L} \approx 8$ and ~25 μm after testing at 523 K at 10^{-2} and 10^{-3} s^{-1}, respectively. It is also apparent in Fig. 9 that there are numerous cavities at the grain boundaries and triple junctions as indicated by the arrows.

4. Discussion

4.1. *The effect of processing temperature on the mechanical strength of Al–Mg alloys*

This investigation demonstrates that HPT processing of an Al–3Mg alloy through 10 turns leads to grain refinement down to ~150 nm in the metal processed at *RT* together with hardening up to a Vickers microhardness of ~180 HV. By contrast, processing at 450 K promotes a less pronounced hardening and grain refinement ($\overline{L} \approx 500$ nm) combined with the development of a more inhomogeneous hardness distribution. These trends are consistent with earlier experiments conducted on other metals processed by HPT at different temperatures [23,76] and with the values reported for Al–Mg alloys having similar Mg content and small additions of Sc [21,22,48,49] although the Al–Mg–Sc alloys consistently exhibit smaller grain sizes.

Plots of Vickers microhardness as a function of equivalent strain (ε_{eq}) [77] were constructed using the hardness values displayed in Fig. 1. The equivalent strain in HPT processing was calculated considering the mean values at the same radial position (*R*), for a given number of turns (*N*), A thickness (*h*) of 0.70 mm was considered in the calculations with the following expression [78]:

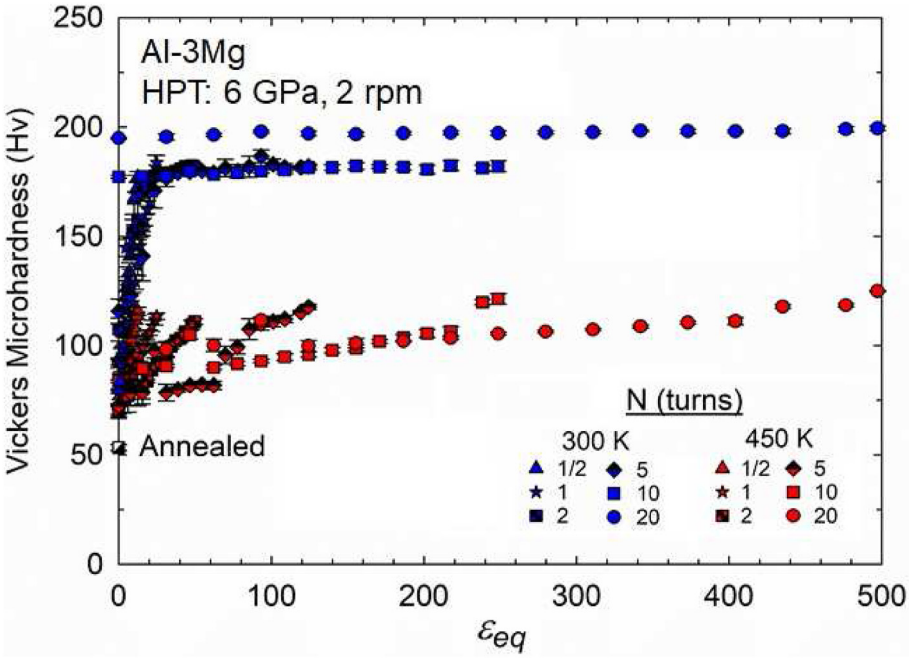

Fig. 10 – Vickers microhardness as a function of equivalent strain for the Al–3Mg alloy processed by HPT at either 300 or 450 K.

$$\varepsilon_{eq} = \frac{2\pi RN}{\sqrt{3}h} \quad (1)$$

The results are shown in Fig. 10 and they demonstrate that the material processed by HPT at *RT* exhibits a fast initial rise in hardness up to a value of ~180 HV for a strain of ~40, followed by an apparent saturation in the hardness values up to 10 revolutions. Nevertheless, there is an increment in the microhardness throughout the entire disc after 20 turns. This hardening behaviour is typical of HPT deformation in metals having low-to-moderate stacking fault energies during processing at low homologous temperatures (T_H) [61,65,79–84]. However, based on the present data it is not possible to confirm that the material reached a full hardness saturation after 20 turns of HPT at *RT*. It should be noted, however, that the hardness values are consistent with earlier experiments with Al–3Mg [65] and Al–3Mg–0.2Sc [61] alloys annealed before HPT processing.

By contrast, the Al–Mg alloy processed by HPT at 450 K displays a very distinct hardening behaviour. Thus, inspection of the variation of the hardness values at the edge positions for different numbers of turns reveals that there is a rapid work hardening up to a peak hardness of ~120 HV at $\varepsilon_{eq} \approx 10$, and this is followed by strain softening down to a hardness of ~75 HV at $\varepsilon_{eq} \approx 80$. The hardness at the edge area again increases and reaches ~120 HV at $\varepsilon_{eq} \approx 120$ and 240, followed by softening to ~110 HV at $\varepsilon_{eq} \approx 80$. This behaviour is consistent with the recurrent oscillations observed in the curve torque vs. time acquired during HPT processing of an Al–3Mg alloy at ~450 K [84].

The microstructural evolution of metals during plastic deformation at high T_H depends upon the prevailing strain rate [85]. It follows from the derivative of Eq. (1) with time that the strain rate in HPT processing is proportional to the rotation rate and the radial position. Also, as demonstrated in Figs. 1 and 10, the hardness in the Al–3Mg alloy processed by HPT at 450 K increases with increasing radii even after 20 turns and the maximum hardness apparently achieved upper bounds at the peripheries of the discs.

Accordingly, based on this hardening behaviour, the different aspect ratios of the grain structures after deformation [23,86] and other literature evidence for an Al–3Mg alloy [84], it is thus revealed that there are two different restoration mechanisms operating in the Al–3Mg alloy during HPT processing at different temperatures. Dynamic restoration at *RT* is connected with a strain-induced grain boundary migration [87–89] whereas HPT processing at 450 K appears to be associated with discontinuous dynamic recrystallization as is typical for conventional metal-working procedures at high homologous temperatures [85].

The influence of grain size on the mechanical strength at low T_H is often predicted using the Hall-Petch relationship [3,4]. This relationship can also be considered for the variation of the Vickers microhardness (H) with the average grain size ($\bar{L}$) as applied in earlier SPD studies [21,65,81,90] using the following equation:

$$H = H_0 + k_H \bar{L}^{-1/2} \quad (2)$$

where H_0 and k_H are material constants.

Fig. 11 displays a plot of Vickers microhardness as a function of $\bar{L}^{-1/2}$ for the Al–3Mg alloy processed by 10 HPT turns in this study considering the hardness at the radial position in which the microstructure was examined. Additional datum points are also included for Al–Mg alloys processed by HPT

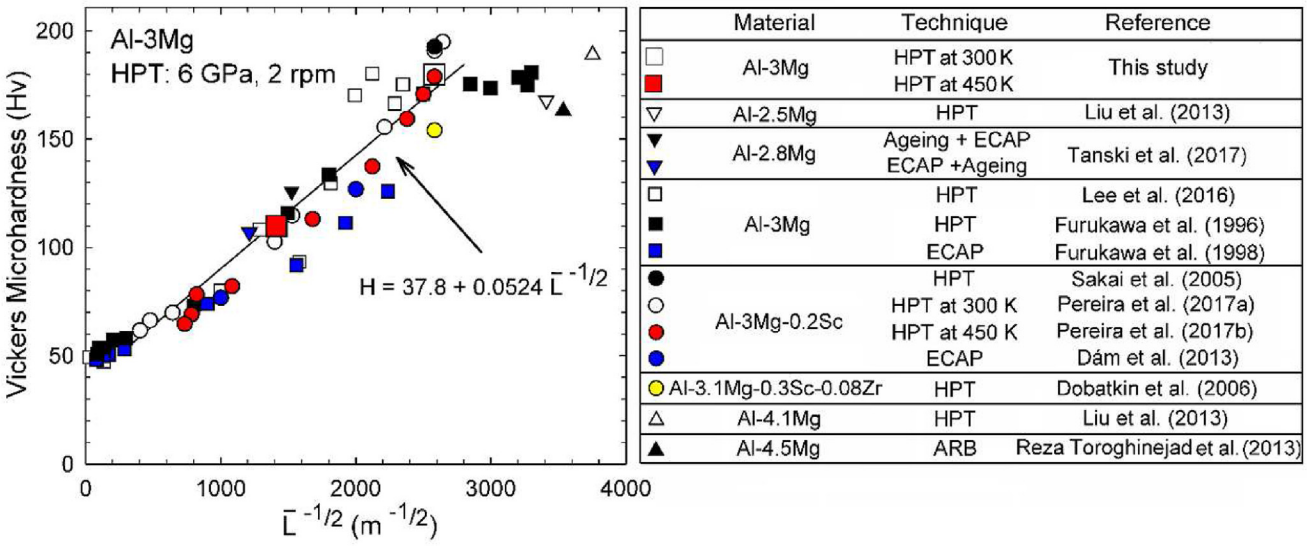

Fig. 11 – Vickers microhardness as a function of $\bar{L}^{-1/2}$ for Al–Mg alloys with similar compositions subjected to either HPT [16,21,48,49,65,69,91,92], ECAP [39,90,93] and ARB [94] at different processing conditions.

[16,21,48,49,65,69,91,92], ECAP [39,90,93] and ARB [94]. It follows from Fig. 11, that although there is some scattering in the datum points for $\bar{L} < 1$ μm, the relationship between H and $\bar{L}^{-1/2}$ follows a linear trend up to $\bar{L}^{-1/2} \approx 2600\ m^{-1/2}$ when the hardness values appear to achieve an upper limit. The scatter in the data is a consequence of the action of additional hardening mechanisms such as dislocation and precipitate strengthening which depend on the thermomechanical history of the Al–Mg alloys. Furthermore, the experimental data up to this point lie close to a single line with $H_0 = 37.8$ HV and $K_H = 0.0524$ HV $m^{-1/2}$.

The results in Fig. 11 indicate also that the processing temperature, the nature of the SPD procedure, the chemical composition and the initial condition prior to processing all affect the mechanical strength in Al–Mg alloys. Processing at higher T_H for a given alloy leads to a larger grain size and lower microhardness due to a faster diffusion kinetics during deformation which favours the elimination of dislocations. Concerning the nature of the SPD method, in general, HPT-processing leads to finer grain structures and higher strength in comparison to other SPD procedures for metals having similar compositions. This occurs because of the higher strains attained by means of HPT processing due to the application of elevated compressive stresses in the disc during deformation [8,10].

It also follows from the results depicted in Fig. 11 that the Al–3Mg–0.2Sc processed through 10 HPT turns at 300 K [48,69] achieves slightly higher hardness values and smaller grain sizes when compared with the Al–3Mg alloy processed by HPT at *RT*. It should be noted, however, that the Al–3Mg–0.2Sc discs were solution treated prior to processing whereas the Al–3Mg used in the current study was annealed before HPT. Consequently, the Al–3Mg alloy exhibited coarse Al_3Mg_2 particles and lower amounts of Mg in solid solution (~2.5% Mg) prior to HPT processing. Conversely, Al_3Mg_2 particles were not detected in the solution-treated Al–3Mg–0.2Sc alloy and the higher amounts of Mg in solid solution in this alloy would reduce the recovery rate and thus permit the attainment of further grain refinement.

This can also explain the larger grain sizes achieved in the Al–3Mg alloy processed by HPT at 450 K compared with the Al–3Mg–0.2Sc deformed under similar conditions. The lower amounts of Mg in solid solution in both the annealed and the HPT-processed alloy increase its stacking fault energy and facilitate dynamic recovery. Additionally, as the mobility of grain boundaries also increases with the lowering of the Mg contents in solid solution [95,96], the transition from the mechanically-driven boundary migration to a discontinuous dynamic recrystallization probably occurs at lower temperatures [87,89].

4.2. *Superplasticity and microstructural stability in Al–Mg alloys*

Superplasticity involves the achievement of elongations ≥400% in crystalline materials having grain sizes <10 μm and with a strain rate sensitivity of ~0.5 [74]. The deformation mechanism associated with superplasticity is GBS where the strain rate at steady-state conditions is given by the following equation [97]:

$$\dot{\varepsilon} = \frac{AD_{gb}Gb}{kT}\left(\frac{b}{d}\right)^2\left(\frac{\sigma}{G}\right)^2 \quad (3)$$

where A is a dimensionless constant, D is the diffusion coefficient for grain boundary diffusion, G is the shear modulus, **b** is the Burgers vector, σ is the applied stress, k is Boltzmann's constant, T is the absolute temperature and d is the spatial grain size calculated as $d \approx 1.74\bar{L}$ [98].

There is consistent evidence supporting the occurrence of GBS in the Al–3Mg alloy processed by 10 HPT revolutions at *RT*

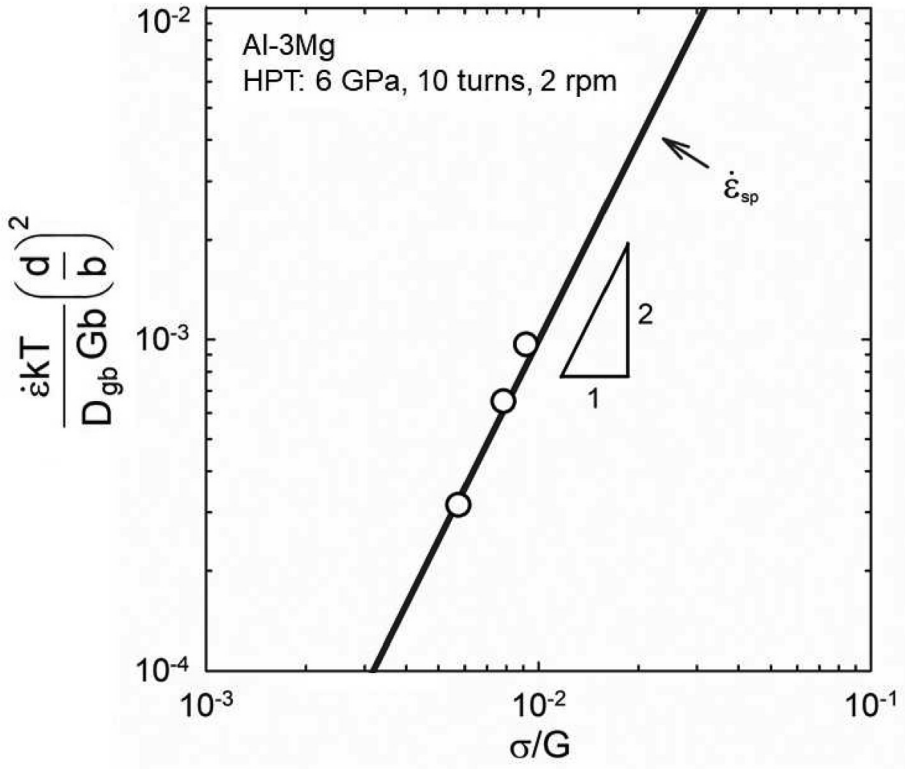

Fig. 12 – Temperature and grain size compensated strain rate as a function of normalized stress for the Al–3Mg alloy processed by HPT at 300 K and tensile tested at 523 K: the solid line corresponds to the theoretical prediction for superplastic flow [97].

during deformation at 523 K. As depicted in Figs. 7 and 8, the 10-HPT-RT material exhibits elongations ≥500% and m values of ~0.5 at strain rates from 10^{-3} to 10^{-2} s^{-1}, reaching a maximum elongation of ~620% for $\dot{\varepsilon} \approx 10^{-3}$ s^{-1}. Conversely, after 10 HPT turns at 450 K the same material attained a maximum elongation of only ~110% due to a low apparent strain rate sensitivity.

It should be noted, however, that the m values estimated from the slope of Fig. 7(b) were calculated using flow stresses at $\varepsilon = 0.1$ and thus considerable grain coarsening may have occurred during heating and deformation up to this stage. Accordingly, and in order to unambiguously confirm the occurrence of superplastic flow in the Al–3Mg alloy processed by HPT at *RT* considering possible grain coarsening effects, Fig. 12 displays the relationship between the temperature and grain size compensated strain rate ($\dot{\varepsilon}\, kT/D_{gb}G\mathbf{b}$) ($d/\mathbf{b}$)^2 and the normalized stress (σ/G) for the material tested at 523 K. In this study, σ was taken as the maximum flow stress and d as the spatial grain size of each specimen after tensile testing at 523 K. The following parameters for pure Al were used in the calculations: $\mathbf{b} = 2.86 \times 10^{-10}$ m, $D_{o,gb} = 1.86 \times 10^{-4}$ m^2 s^{-1}, $Q_{gb} = 86$ kJ mol^{-1}, G (MPa) = (3.022×10^4) - 16T [99]. The line labelled $\dot{\varepsilon}_{sp}$ corresponds to the theoretical prediction of the rate of superplasticity using Eq. (3) with $A = 10$ [97].

The results in Fig. 12 confirm that there is an excellent agreement between the experimental data and the theoretical model for superplasticity involving a stress exponent of 2 and therefore it is concluded that the superplastic flow is governed by GBS accommodated by intragranular slip through dislocation climb in the Al–3Mg alloy [97]. Furthermore, as grain coarsening often occurs during tensile testing at elevated temperatures, it is shown that a reliable procedure for applying Eq. (3) involves measurements of the grain size in the gauge sections of the fractured specimens combined with use of the maximum stresses during testing.

The superior superplastic characteristics of the Al–3Mg alloy processed by HPT at 300 K derive from its smaller grain size as well as its greater microstructural stability in relation to the same material processed at 450 K. This is supported by data in Fig. 9(a) and (b) which show that the microstructure of the 10-HPT-RT metal after deformation at 523 K consists of a homogeneous array of fairly equiaxed grains with average sizes of ~1–2 μm. Hence, superplastic flow occurs in the Al–3Mg alloy at a low homologous temperature ($T_H \approx 0.56$) and at high strain rates up to 10^{-2} s^{-1}. By contrast to this result, Fig. 9(c) and (d) suggest the occurrence of abnormal grain growth in the material originally processed by HPT at 450 K and further tested in tension at 523 K.

The enhanced thermal stability in the Al–3Mg alloy after HPT at *RT* shows reasonable agreement with experimental evidence of low temperature superplasticity in the HPT-processed Al–3Mg–0.2Sc alloy [21,22,45]. It is noted that the microstructures of these alloys prior to processing and after 10 HPT turns are very distinct as Al_3Mg_2 particles are clearly distinguished in the annealed Al–3Mg alloy and their

formation is prevented by the initial solution treatment in the Al–3Mg–0.2Sc alloy.

It is well-established that the migration of high-angle grain boundaries (HAGBs) during recrystallization for severely deformed metals is primarily driven by the energy decrease associated with the elimination of dislocations and grain contours [85]. The driving pressure for recrystallization is similar for both Al–Mg alloys after 10 HPT turns at *RT* ($\overline{L} \approx 150$ nm) [48,69] but nevertheless finely dispersed precipitates hinder the moving boundaries due to the Zener pinning pressure and reduce the rate of migration [96,100]. Therefore, whereas precipitation of nanosized Al_3Sc is recognised to be the main cause for the remarkable microstructural stability of Al–Sc alloys [18,36,42,101,102], the presence of Al_3Mg_2 precipitates with an average size of 10 nm is responsible for delaying the migration rate of HAGBs and permitting the attainment of superplastic elongations at 523 K in the Al–3Mg alloy. This represents an economical advantage for using Al–Mg alloys without any Sc addition as this rare earth element is expensive and scarcely available [19].

The microstructures of the Al–3Mg alloy processed at 450 K displayed coarser precipitates (~16 nm in diameter) and a more heterogeneous distribution of grains with an average size of ~500 nm. The comparatively higher diffusion rate at this processing temperature and continuous straining during HPT processing apparently led to a partial dissolution and coalescence of the precipitates as previously observed also in other Al alloy processed by HPT at different temperatures [68]. Consequently, there may exist regions where the lower numbers of precipitates and their coarser sizes may allow a faster migration rate of boundaries during heating and deformation at high temperatures [96].

Furthermore, the hardness measurements and the TEM analysis showed that the microstructure of the Al–3Mg alloy after HPT at 450 K is more heterogeneous than after processing at 300 K. Accordingly, boundaries of the larger grains tend to migrate towards more deformed regions which display a higher driving pressure compared with the areas with lower hardness. This leads to the existence of abnormal ultrafine-grained structures which may be attributed to the inherent microstructural heterogeneity in the Al–3Mg alloy after HPT at 450 K together with a reduced Zener pinning effect during heating to the testing temperature.

Finally, it should be noted that the rise in the processing temperature may also affect the material microtexture [84,103] and increase the fraction of boundaries having high mobility. This topic will require further investigation in future studies.

5. Summary and conclusions

An annealed Al–3Mg alloy with an average grain size of ~300 μm was subjected to up to 20 turns of HPT at either room temperature (*RT*) or 450 K. Thereafter, the alloy processed through 10 turns was tested in tension at *RT* and 523 K to investigate the effect of the HPT processing temperature on the flow behaviour and microstructural stability.

1 A reasonably homogeneous distribution of Vickers microhardness was achieved in the Al–3Mg alloy after 10 HPT turns at *RT* with an average value of ~180 HV. Conversely, the hardening behaviour during HPT at 450 K showed a marked strain rate dependence where the metal exhibited an inhomogeneous hardness distribution with higher values reaching ~120 HV at the disc edges even after 20 revolutions. This suggests a more prominent contribution of thermally-assisted mechanisms during HPT at 450 K.
2 After 10 HPT turns at *RT*, the Al–3Mg alloy displayed an array of slightly elongated grains with an average size of $\overline{L} \approx 150$ nm, a dislocation density of ~10^{15} m^{-2} and a dispersion of Al_3Mg_2 particles with diameters of ~10 nm. These results are consistent with the flow stresses exceeding 650 MPa and the negligible ductility at *RT*. By contrast, HPT at 450 K led to a tensile strength of only ~220 MPa due to the development of equiaxed grains ($\overline{L} \approx 500$ nm), larger precipitates and a dislocation density of ~3×10^{14} m^{-2} after 10 revolutions.
3 The Al–3Mg alloy processed by 10 HPT turns at *RT* achieved superplastic elongations ≥500% when tensile tested at 523 K, reaching a maximum elongation of ~620% for $\dot{\varepsilon} \approx 10^{-3}$ s^{-1}. These unusual ductilities at a low homologous temperature are attributed to an enhanced thermal stability due to the formation of a homogenous microstructure after HPT and the pinning of grain boundaries by Al_3Mg_2 precipitates.
4 The material processed by 10 HPT turns at 450 K and further tested in tension at 523 K exhibited a bimodal distribution of grains having large grains with tens of micrometres in size surrounded by ultrafine grains. Accordingly, the onset of abnormal coarsening led to a low strain rate sensitivity and thus low elongations during deformation at 523 K for strain rates in the range of 10^{-3} to 10^{-2} s^{-1}.

Data availability

The data required to reproduce these findings can be shared upon request.

Declaration of competing interest

The authors declare that they have no known competing financial interests or personal relationships that could have appeared to influence the work reported in this paper.

Acknowledgements

The authors thank the Microscopy Centre of UFMG for the support in the electron microscopy analysis. This research was sponsored by CNPq under Grants 443736/2018–9 (PHRP) and 300874/2018–9 (PRC), and FAPEMIG under Projects APQ-01342-21 (PHRP) and APQ 02133/22 (PCAF). The work of two of us was supported by the European Research Council under ERC Grant Agreement No. 267464-SPDMETALS (YH and TGL).

REFERENCES

[1] Valiev RZ, Islamgaliev RK, Alexandrov IV. Bulk nanostructured materials from severe plastic deformation. Prog Mater Sci 2000;45:103–89. https://doi.org/10.1016/S0079-6425(99)00007-9.

[2] Langdon TG. Twenty-five years of ultrafine-grained materials: achieving exceptional properties through grain refinement. Acta Mater 2013;61:7035–59. https://doi.org/10.1016/j.actamat.2013.08.018.

[3] Hall EO. The deformation and ageing of mild steel: III discussion of results. Proc Phys Soc B 1951;64:747–53. https://doi.org/10.1088/0370-1301/64/9/303.

[4] Petch NJ. The cleavage strength of polycrystals. J Iron Steel Inst 1953;174:25–8. https://doi.org/10.1007/BF01972547.

[5] Edalati K, Horita Z. A review on high-pressure torsion (HPT) from 1935 to 1988. Mater Sci Eng 2016;652:325–52. https://doi.org/10.1016/j.msea.2015.11.074.

[6] Zhilyaev AP, Langdon TG. Using high-pressure torsion for metal processing: fundamentals and applications. Prog Mater Sci 2008;53:893–979. https://doi.org/10.1016/j.pmatsci.2008.03.002.

[7] Hohenwarter A, Bachmaier A, Gludovatz B, Scheriau S, Pippan R. Technical parameters affecting grain refinement by high pressure torsion. Int J Mater Res 2009;100:1653–61. https://doi.org/10.3139/146.110224.

[8] Pereira PHR, Figueiredo RB. Finite element modelling of high-pressure torsion: an overview. Mater Trans 2019;60:1139–50. https://doi.org/10.2320/matertrans.MF201906.

[9] Pereira PHR, Figueiredo RB, Cetlin PR, Langdon TG. An examination of the elastic distortions of anvils in high-pressure torsion. Mater Sci Eng 2015;631:201–8. https://doi.org/10.1016/j.msea.2015.02.052.

[10] Pereira PHR, Figueiredo RB, Cetlin PR, Langdon TG. Using finite element modelling to examine the flow process and temperature evolution in HPT under different constraining conditions. IOP Conf Ser Mater Sci Eng 2014;63:012041. https://doi.org/10.1088/1757-899X/63/1/012041.

[11] Pereira PHR, Figueiredo RB, Huang Y, Cetlin PR, Langdon TG. Modeling the temperature rise in high-pressure torsion. Mater Sci Eng 2014;593:185–8. https://doi.org/10.1016/j.msea.2013.11.015.

[12] Edalati K, Hashiguchi Y, Pereira PHR, Horita Z, Langdon TG. Effect of temperature rise on microstructural evolution during high-pressure torsion. Mater Sci Eng 2018;714:167–71. https://doi.org/10.1016/j.msea.2017.12.095.

[13] Figueiredo RB, Pereira PHR, Aguilar MTP, Cetlin PR, Langdon TG. Using finite element modeling to examine the temperature distribution in quasi-constrained high-pressure torsion. Acta Mater 2012;60:3190–8. https://doi.org/10.1016/j.actamat.2012.02.027.

[14] Figueiredo RB, Cetlin PR, Langdon TG. Using finite element modeling to examine the flow processes in quasi-constrained high-pressure torsion. Mater Sci Eng 2011;528:8198–204. https://doi.org/10.1016/j.msea.2011.07.040.

[15] Wang J, Furukawa M, Horita Z, Nemoto M, Valiev RZ, Langdon TG. Enhanced grain growth in an Al-Mg alloy with ultrafine grain size. Mater Sci Eng, A 1996;216:41–6. https://doi.org/10.1016/0921-5093(96)10390-7.

[16] Wang J, Iwahashi Y, Horita Z, Furukawa M, Nemoto M, Valiev RZ, et al. An investigation of microstructural stability in an Al-Mg alloy with submicrometer grain size. Acta Mater 1996;44:2973–82. https://doi.org/10.1016/1359-6454(95)00395-9.

[17] Hasegawa H, Komura S, Utsunomiya A, Horita Z, Furukawa M, Nemoto M, et al. Thermal stability of ultrafine-grained aluminum in the presence of Mg and Zr additions. Mater Sci Eng, A 1999;265:188–96. https://doi.org/10.1016/S0921-5093(98)01136-8.

[18] Komura S, Horita Z, Furukawa M, Nemoto M, Langdon TG. Influence of scandium on superplastic ductilities in an Al-Mg-Sc alloy. J Mater Res 2000;15:2571–6. https://doi.org/10.1557/JMR.2000.0367.

[19] Røyset J, Ryum N. Scandium in aluminium alloys. Int Mater Rev 2005;50:19–44. https://doi.org/10.1179/174328005X14311.

[20] Duan Y, Xu G, Zhou L, Xiao D, Deng Y, Yin Z, et al. Achieving high superplasticity of a traditional thermal-mechanical processed non-superplastic Al-Zn-Mg alloy sheet by low Sc additions. J Alloys Compd 2015;638:364–73. https://doi.org/10.1016/j.jallcom.2015.03.090.

[21] Pereira PHR, Huang Y, Langdon TG. Examining the microhardness evolution and thermal stability of an Al–Mg–Sc alloy processed by high-pressure torsion at a high temperature. J Mater Res Technol 2017;6:348–54. https://doi.org/10.1016/j.jmrt.2017.05.008.

[22] Pereira PHR, Huang Y, Langdon TG. Thermal stability and superplastic behaviour of an Al-Mg-Sc alloy processed by ECAP and HPT at different temperatures. IOP Conf Ser Mater Sci Eng 2017;194:012013. https://doi.org/10.1088/1757-899X/194/1/012013.

[23] Ghosh P, Renk O, Pippan R. Microtexture analysis of restoration mechanisms during high pressure torsion of pure nickel. Mater Sci Eng 2017;684:101–9. https://doi.org/10.1016/j.msea.2016.12.032.

[24] Abramova MM, Enikeev NA, Sauvage X, Etienne A, Radiguet B, Ubyivovk E, et al. Thermal stability and extra-strength of an ultrafine grained stainless steel produced by high pressure torsion. Rev Adv Mater Sci 2015;43:83–8.

[25] Dobatkin SV, Rybalchenko OV, Enikeev NA, Tokar AA, Abramova MM. Formation of fully austenitic ultrafine-grained high strength state in metastable Cr-Ni-Ti stainless steel by severe plastic deformation. Mater Lett 2016;166:276–9. https://doi.org/10.1016/j.matlet.2015.12.094.

[26] Flausino PCA, Corrêa ECS, Pereira PHR, Aguilar MTP, Cetlin PR. Thermal stability of copper processed by multidirectional forging: effect of deformation amplitude and cumulative strain. Mater Sci Eng, A 2022;846:143299. https://doi.org/10.1016/J.MSEA.2022.143299.

[27] Flausino PCA, Nassif MEL, de Castro Bubani F, Pereira PHR, Aguilar MTP, Cetlin PR. Microstructural evolution and mechanical behavior of copper processed by low strain amplitude multi-directional forging. Mater Sci Eng, A 2019;756:474–83. https://doi.org/10.1016/j.msea.2019.04.075.

[28] Flausino PCA, Nassif MEL, Bubani FDC, Pereira PHR, Aguilar MTP, Cetlin PR. Influence of strain amplitude on the microstructural evolution and flow properties of copper processed by multidirectional forging. Adv Eng Mater 2020;22:1901510. https://doi.org/10.1002/adem.201901510.

[29] Sauvage X, Duchaussoy A, Zaher G. Strain induced segregations in severely deformed materials. Mater Trans 2019;60:1151–8. https://doi.org/10.2320/matertrans.MF201919.

[30] Abdeljawad F, Foiles SM. Stabilization of nanocrystalline alloys via grain boundary segregation: a diffuse interface model. Acta Mater 2015;101:159–71. https://doi.org/10.1016/j.actamat.2015.07.058.

[31] de Oliveira PC, Montoro LA, Perez-Prado MT, Hohenwarter A, Figueiredo RB, Isaac A. Development of segregations in a Mg–Mn–Nd alloy during HPT processing. Mater Sci Eng 2021;802:140423. https://doi.org/10.1016/j.msea.2020.140423.

[32] Devaraj A, Wang W, Vemuri R, Kovarik L, Jiang X, Bowden M, et al. Grain boundary segregation and

intermetallic precipitation in coarsening resistant nanocrystalline aluminum alloys. Acta Mater 2019;165:698–708. https://doi.org/10.1016/j.actamat.2018.09.038.
[33] Sha G, Yao L, Liao X, Ringer SP, Duan ZC, Langdon TG. Segregation of solute elements at grain boundaries in an ultrafine grained Al-Zn-Mg-Cu alloy. Ultramicroscopy 2011;111:500–5. https://doi.org/10.1016/j.ultramic.2010.11.013.
[34] Zhang Y, Jin S, Trimby PW, Liao X, Murashkin MY, Valiev RZ, et al. Dynamic precipitation, segregation and strengthening of an Al-Zn-Mg-Cu alloy (AA7075) processed by high-pressure torsion. Acta Mater 2019;162:19–32. https://doi.org/10.1016/j.actamat.2018.09.060.
[35] dos Santos IC, Mazzer EM, Figueiredo RB, Langdon TG, Pereira PHR. Evidence for two-stage hardening in an Al-Zn-Mg-Cu alloy processed by high-pressure torsion. J Alloys Compd 2023:941. https://doi.org/10.1016/j.jallcom.2023.168839. 10.1016.
[36] Jones MJ, Humphreys FJ. Interaction of recrystallization and precipitation: the effect of Al3Sc on the recrystallization behaviour of deformed aluminium. Acta Mater 2003;51:2149–59. https://doi.org/10.1016/S1359-6454(03)00002-8.
[37] Marquis EA, Seidman DN. Nanoscale structural evolution of Al3Sc precipitates in Al(Sc) alloys. Acta Mater 2001;49:1909–19. https://doi.org/10.1016/S1359-6454(01)00116-1.
[38] Málek P, Turba K, Cieslar M, Drbohlav I, Kruml T. Structure development during superplastic deformation of an Al-Mg-Sc-Zr alloy. Mater Sci Eng 2007;462:95–9. https://doi.org/10.1016/j.msea.2006.01.171.
[39] Dám K, Lejček P, Michalcová A. In situ TEM investigation of microstructural behavior of superplastic Al-Mg-Sc alloy. Mater Char 2013;76:69–75. https://doi.org/10.1016/j.matchar.2012.12.005.
[40] Mikhaylovskaya AV, Yakovtseva OA, Cheverikin VV, Kotov AD, Portnoy VK. Superplastic behaviour of Al-Mg-Zn-Zr-Sc-based alloys at high strain rates. Mater Sci Eng, A 2016;659:225–33. https://doi.org/10.1016/j.msea.2016.02.061.
[41] Pereira PHR, Huang Y, Langdon TG. Examining the mechanical properties and superplastic behaviour in an Al-Mg-Sc alloy after processing by HPT. Letters on Materials 2015;5:294–300.
[42] Komura S, Horita Z, Furukawa M, Nemoto M, Langdon TG. An evaluation of the flow behavior during high strain rate superplasticity in an Al-Mg-Sc alloy. Metall Mater Trans A Phys Metall Mater Sci 2001;32:707–16. https://doi.org/10.1007/s11661-001-1006-9.
[43] Liu FC, Ma ZY. Achieving exceptionally high superplasticity at high strain rates in a micrograined Al-Mg-Sc alloy produced by friction stir processing. Scripta Mater 2008;59:882–5. https://doi.org/10.1016/j.scriptamat.2008.06.035.
[44] Avtokratova E, Sitdikov O, Markushev M, Mulyukov R. Extraordinary high-strain rate superplasticity of severely deformed Al–Mg–Sc–Zr alloy. Mater Sci Eng, A 2012;538:386–90. https://doi.org/10.1016/j.msea.2012.01.041.
[45] Pereira PHR, Huang Y, Kawasaki M, Langdon TG. An examination of the superplastic characteristics of Al–Mg–Sc alloys after processing. J Mater Res 2017;32:4541–53. https://doi.org/10.1557/jmr.2017.286.
[46] Sitdikov O, Avtokratova E, Sakai T, Tsuzaki K, Kaibyshev R, Watanabe Y. Effect of processing temperature on microstructure development during ECAP of Al-Mg-Sc alloy. Mater Sci Forum 2008;584–586:481–6. https://doi.org/10.4028/www.scientific.net/MSF.584-586.481.
[47] Sitdikov O, Avtokratova E, Babicheva R. Effect of temperature on the formation of a microstructure upon equal-channel angular pressing of the Al-Mg-Sc 1570 alloy. Phys Met Metallogr 2010;110:153–61. https://doi.org/10.1134/S0031918X10080053.
[48] Pereira PHR, Huang Y, Langdon TG. Examining the thermal stability of an Al-Mg-Sc alloy processed by high-pressure torsion. Mater Res 2017;20:39–45. https://doi.org/10.1590/1980-5373-MR-2017-0207.
[49] Dobatkin SV, Zakharov VV, Ayu Vinogradov, Kitagawa K, Krasil'nikov NA, Rostova TD, et al. Nanocrystalline structure formation in Al-Mg-Sc alloys during severe plastic deformation, vol. 2006. Russian Metallurgy (Metally); 2006. p. 533–40. https://doi.org/10.1134/S0036029506060115.
[50] Mohammadi A, Enikeev NA, Murashkin MY, Arita M, Edalati K. Developing age-hardenable Al-Zr alloy by ultra-severe plastic deformation: significance of supersaturation, segregation and precipitation on hardening and electrical conductivity. Acta Mater 2021;203:116503. https://doi.org/10.1016/j.actamat.2020.116503.
[51] Xu C, Furukawa M, Horita Z, Langdon TG. Using ECAP to achieve grain refinement, precipitate fragmentation and high strain rate superplasticity in a spray-cast aluminum alloy. Acta Mater 2003;51:6139–49. https://doi.org/10.1016/S1359-6454(03)00433-6.
[52] Liddicoat PV, Liao XZ, Zhao Y, Zhu Y, Murashkin MY, Lavernia EJ, et al. Nanostructural hierarchy increases the strength of aluminium alloys. Nat Commun 2010;1. https://doi.org/10.1038/ncomms1062.
[53] Sauvage X, Enikeev N, Valiev RZ, Nasedkina Y, Murashkin M. Atomic-scale analysis of the segregation and precipitation mechanisms in a severely deformed Al-Mg alloy. Acta Mater 2014;72:125–36. https://doi.org/10.1016/j.actamat.2014.03.033.
[54] Zhang Y, Jin S, Trimby P, Liao X, Murashkin MY, Valiev RZ, et al. Strengthening mechanisms in an ultrafine-grained Al-Zn-Mg-Cu alloy processed by high pressure torsion at different temperatures. Mater Sci Eng, A 2019;752:223–32. https://doi.org/10.1016/j.msea.2019.02.094.
[55] Hohl J, Kumar P, Misra M, Menezes P, Mushongera LT. Thermodynamic stabilization of nanocrystalline aluminum. J Mater Sci 2021;56:14611–23. https://doi.org/10.1007/s10853-021-06224-2.
[56] Pun SC, Wang W, Khalajhedayati A, Schuler JD, Trelewicz JR, Rupert TJ. Nanocrystalline Al-Mg with extreme strength due to grain boundary doping. Mater Sci Eng, A 2017;696:400–6. https://doi.org/10.1016/j.msea.2017.04.095.
[57] Koju RK, Mishin Y. Atomistic study of grain-boundary segregation and grain-boundary diffusion in Al-Mg alloys. Acta Mater 2020;201:596–603. https://doi.org/10.1016/J.ACTAMAT.2020.10.029.
[58] Figueiredo RB, Langdon TG. Development of structural heterogeneities in a magnesium alloy processed by high-pressure torsion. Mater Sci Eng 2011;528:4500–6. https://doi.org/10.1016/j.msea.2011.02.048.
[59] Kai M, Horita Z, Langdon TG. Developing grain refinement and superplasticity in a magnesium alloy processed by high-pressure torsion. Mater Sci Eng 2008;488:117–24. https://doi.org/10.1016/j.msea.2007.12.046.
[60] Ribárik G, Gubicza J, Ungár T. Correlation between strength and microstructure of ball-milled Al-Mg alloys determined by X-ray diffraction. Mater Sci Eng 2004:387–9. https://doi.org/10.1016/j.msea.2004.01.089.
[61] Pereira PHR, Huang Y, Langdon TG. Influence of initial heat treatment on the microhardness evolution of an Al-Mg-Sc alloy processed by high-pressure torsion. Mater Sci Forum

2016;879:1471–6. https://doi.org/10.4028/www.scientific.net/MSF.879.1471.
[62] Shahmir H, Pereira PHR, Huang Y, Langdon TG. Mechanical properties and microstructural evolution of nanocrystalline titanium at elevated temperatures. Mater Sci Eng, A 2016;669:358–66. https://doi.org/10.1016/j.msea.2016.05.105.
[63] Gubicza J, Pereira PHR, Kapoor G, Huang Y, Vadlamani SS, Langdon TG. Annealing-induced hardening in ultrafine-grained Ni-Mo alloys. Adv Eng Mater 2018. https://doi.org/10.1002/adem.201800184.
[64] Figueiredo RB, Sabbaghianrad S, Giwa A, Greer JR, Langdon TG. Evidence for exceptional low temperature ductility in polycrystalline magnesium processed by severe plastic deformation. Acta Mater 2017;122:322–31. https://doi.org/10.1016/j.actamat.2016.09.054.
[65] Lee H-J, Han J-K, Janakiraman S, Ahn B, Kawasaki M, Langdon TG. Significance of grain refinement on microstructure and mechanical properties of an Al-3% Mg alloy processed by high-pressure torsion. J Alloys Compd 2016;686. https://doi.org/10.1016/j.jallcom.2016.06.194.
[66] Korneva A, Straumal B, Kilmametov A, Chulist R, Cios G, Baretzky B, et al. Dissolution of Ag precipitates in the Cu-8wt.%Ag alloy deformed by high pressure torsion. Materials (Basel) 2019;12:1–12. https://doi.org/10.3390/ma12030447.
[67] Cerri E, Leo P. Influence of severe plastic deformation on aging of Al-Mg-Si alloys. Mater Sci Eng 2005;410–411:226–9. https://doi.org/10.1016/j.msea.2005.08.135.
[68] Xue K, Wang B, Yan S, Bo D, Li P. Strain-induced dissolution and precipitation of secondary phases and synergetic strengthening mechanisms of Al–Zn–Mg–Cu alloy during ECAP. Adv Eng Mater 2019;21:1801182. https://doi.org/10.1002/adem.201801182.
[69] Sakai G, Horita Z, Langdon TG. Grain refinement and superplasticity in an aluminum alloy processed by high-pressure torsion. Mater Sci Eng, A 2005;393:344–51. https://doi.org/10.1016/j.msea.2004.11.007.
[70] Lage MDA, Soares RB, Pereira PHR, Figueiredo RB, Lins VFC, Langdon TG. Effect of high-pressure torsion on corrosion behavior of a solution-treated Al-Mg-Sc alloy in a saline solution. Mater Res 2019;22. https://doi.org/10.1590/1980-5373-MR-2019-0343.
[71] Mathew RT, Singam S, Ghosh P, Masa SK, Prasad MJNV. The defining role of initial microstructure and processing temperature on microstructural evolution, hardness and tensile response of Al-Mg-Sc-Zr (AA5024) alloy processed by high pressure torsion. J Alloys Compd 2022;901:163548. https://doi.org/10.1016/j.jallcom.2021.163548.
[72] Pereira PHR, Wang YC, Huang Y, Langdon TG. Influence of grain size on the flow properties of an Al-Mg-Sc alloy over seven orders of magnitude of strain rate. Mater Sci Eng 2017;685:367–76. https://doi.org/10.1016/j.msea.2017.01.020.
[73] Kawasaki M, Langdon TG. Review: achieving superplasticity in metals processed by high-pressure torsion. J Mater Sci 2014;49:6487–96. https://doi.org/10.1007/s10853-014-8204-5.
[74] Langdon TG. Seventy-five years of superplasticity: historic developments and new opportunities. J Mater Sci 2009;44:5998–6010. https://doi.org/10.1007/s10853-009-3780-5.
[75] Langdon TG. An evaluation of the strain contributed by grain boundary sliding in superplasticity. Mater Sci Eng, A 1994;174:225–30. https://doi.org/10.1016/0921-5093(94)91092-8.
[76] Edalati K, Horita Z. Significance of homologous temperature in softening behavior and grain size of pure metals processed by high-pressure torsion. Mater Sci Eng 2011;528:7514–23. https://doi.org/10.1016/j.msea.2011.06.080.
[77] Vorhauer A, Pippan R. On the homogeneity of deformation by high pressure torsion. Scripta Mater 2004;51:921–5. https://doi.org/10.1016/j.scriptamat.2004.04.025.
[78] Valiev RZ, Ivanisenko YV, Rauch EF, Baudelet B. Structure and deformaton behaviour of Armco iron subjected to severe plastic deformation. Acta Mater 1996;44:4705–12. https://doi.org/10.1016/S1359-6454(96)00156-5.
[79] Andreau O, Gubicza J, Xian Zhang N, Huang Y, Jenei P, Langdon TG. Effect of short-term annealing on the microstructures and flow properties of an Al-1% Mg alloy processed by high-pressure torsion. Mater Sci Eng 2014;615:231–9. https://doi.org/10.1016/j.msea.2014.07.018.
[80] Loucif A, Figueiredo RB, Baudin T, Brisset F, Chemam R, Langdon TG. Ultrafine grains and the Hall-Petch relationship in an Al-Mg-Si alloy processed by high-pressure torsion. Mater Sci Eng 2012;532:139–45. https://doi.org/10.1016/j.msea.2011.10.074.
[81] Bazarnik P, Huang Y, Lewandowska M, Langdon TG. Structural impact on the Hall-Petch relationship in an Al-5Mg alloy processed by high-pressure torsion. Mater Sci Eng 2015;626:9–15. https://doi.org/10.1016/j.msea.2014.12.027.
[82] Edalati K, Akama D, Nishio A, Lee S, Yonenaga Y, Cubero-Sesin JM, et al. Influence of dislocation-solute atom interactions and stacking fault energy on grain size of single-phase alloys after severe plastic deformation using high-pressure torsion. Acta Mater 2014;69:68–77. https://doi.org/10.1016/j.actamat.2014.01.036.
[83] Kawasaki M. Different models of hardness evolution in ultrafine-grained materials processed by high-pressure torsion. J Mater Sci 2014;49:18–34. https://doi.org/10.1007/s10853-013-7687-9.
[84] Bachmaier A, Hafok M, Pippan R. Rate independent and rate dependent structural evolution during severe plastic deformation. Mater Trans 2010;51. https://doi.org/10.2320/matertrans.MB200912.
[85] Sakai T, Belyakov A, Kaibyshev R, Miura H, Jonas JJ. Dynamic and post-dynamic recrystallization under hot, cold and severe plastic deformation conditions. Prog Mater Sci 2014;60:130–207. https://doi.org/10.1016/j.pmatsci.2013.09.002.
[86] Vorhauer A, Pippan R. On the onset of a steady state in body-centered cubic iron during severe plastic deformation at low homologous temperatures. Metall Mater Trans A Phys Metall Mater Sci 2008;39:417–29. https://doi.org/10.1007/s11661-007-9413-1.
[87] Renk O, Pippan R. Transition from thermally assisted to mechanically driven boundary migration and related apparent activation energies. Scripta Mater 2018;154:212–5. https://doi.org/10.1016/j.scriptamat.2018.05.052.
[88] Pippan R, Scheriau S, Taylor A, Hafok M, Hohenwarter A, Bachmaier A. Saturation of fragmentation during severe plastic deformation. Annu Rev Mater Res 2010;40:319–43. https://doi.org/10.1146/annurev-matsci-070909-104445.
[89] Renk O, Pippan R. Saturation of grain refinement during severe plastic deformation of single phase materials: reconsiderations, current status and open questions. Mater Trans 2019;60:1270–82. https://doi.org/10.2320/matertrans.MF201918.
[90] Furukawa M, Horita Z, Nemoto M, Valiev RZ, Langdon TG. Factors influencing the flow and hardness of materials with ultrafine grain sizes. Philos Mag A 1998;78:203–16. https://doi.org/10.1080/014186198253769.
[91] Furukawa M, Horita Z, Nemoto M, Valiev RZ, Langdon TG. Microhardness measurements and the hall-petch relationship in an Al-Mg alloy with submicrometer grain size. Acta Mater 1996;44:4619–29. https://doi.org/10.1016/1359-6454(96)00105-X.

[92] Liu MP, Roven HJ, Murashkin MY, Valiev RZ, Kilmametov A, Zhang Z, et al. Structure and mechanical properties of nanostructured Al-Mg alloys processed by severe plastic deformation. J Mater Sci 2013;48:4681–8. https://doi.org/10.1007/S10853-012-7133-4.

[93] Tański T, Snopiński P, Prusik K, Sroka M. The effects of room temperature ECAP and subsequent aging on the structure and properties of the Al-3%Mg aluminium alloy. Mater Char 2017;133:185–95. https://doi.org/10.1016/j.matchar.2017.09.039.

[94] Reza Toroghinejad M, Ashrafizadeh F, Jamaati R. On the use of accumulative roll bonding process to develop nanostructured aluminum alloy 5083. Mater Sci Eng 2013;561:145–51. https://doi.org/10.1016/j.msea.2012.11.010.

[95] Huang Y, Humphreys FJ. The effect of solutes on grain boundary mobility during recrystallization and grain growth in some single-phase aluminium alloys. Mater Chem Phys 2012;132:166–74. https://doi.org/10.1016/J.MATCHEMPHYS.2011.11.018.

[96] Humphreys FJ, Hatherly M. Recrystallization and related annealing phenomena. second ed. Oxford: Pergamon Press; 2004. https://doi.org/10.1016/B978-0-08-044164-1.X5000-2.

[97] Langdon TG. A unified approach to grain boundary sliding in creep and superplasticity. Acta Metall Mater 1994;42:2437–43. https://doi.org/10.1016/0956-7151(94)90322-0.

[98] Mohamed FA, Langdon TG. Creep at low stress levels in the superplastic Zn-22% Al eutectoid. Acta Metall 1975;23:117–24. https://doi.org/10.1016/0001-6160(75)90076-0.

[99] Mohamed FA, Langdon TG. Deformation mechanism maps based on grain size. Metall Trans A 1974;5:2339–45. https://doi.org/10.1007/BF02644014.

[100] Humphreys FJ. A unified theory of recovery, recrystallization and grain growth, based on the stability and growth of cellular microstructures - II. The effect of second-phase particles. Acta Mater 1997;45:5031–9. https://doi.org/10.1016/S1359-6454(97)00173-0.

[101] Komura S, Furukawa M, Horita Z, Nemoto M, Langdon TG. Optimizing the procedure of equal-channel angular pressing for maximum superplasticity. Mater Sci Eng 2001;297:111–8. https://doi.org/10.1016/S0921-5093(00)01255-7.

[102] Komura S, Berbon PB, Furukawa M, Horita Z, Nemoto M, Langdon TG. High strain rate superplasticity in an Al-Mg alloy containing scandium. Scripta Mater 1998;38:1851–6. https://doi.org/10.1016/S1359-6462(98)00099-2.

[103] Azzeddine H, Bradai D, Baudin T, Langdon TG. Texture evolution in high-pressure torsion processing. Prog Mater Sci 2022;125. https://doi.org/10.1016/j.pmatsci.2021.100886.